

Testing a coupled hydro-thermo-chemo-geomechanical model for gas hydrate bearing sediments using triaxial compression lab experiments

SHUBHANGI GUPTA* , CHRISTIAN DEUSNER†, MATTHIAS HAECKEL‡, RAINER HELMIG‡, and BARBARA WOHLMUTH*

The presence of gas hydrates influences the stress-strain behavior and increases the load-bearing capacity of sub-marine sediments. This stability is reduced or completely lost when gas hydrates become unstable. Since natural gas hydrate reservoirs are considered as potential resources for gas production on industrial scales, there is a very strong need for numerical production simulators with geomechanical capabilities. To reliably predict the mechanical behavior of gas hydrate-bearing sediments during gas production, numerical tools must be sufficiently calibrated against data from controlled experiments or field tests, and the models must consider thermo-hydro-chemo-mechanical process coupling in a suitable manner. In this study, we perform a controlled triaxial volumetric strain test on a sediment sample in which methane hydrate is first formed under controlled isotropic effective stress and then dissociated via depressurization under controlled total stress. Sample deformations were kept small, and under these constraints, we assume that concepts of poro-elasticity are essentially valid. We numerically simulate this experiment using a hydro-geomechanical hydrate reservoir code. The results show that the dynamic coupling between transport, reaction, and mechanical processes during methane hydrate formation and dissociation in sandy sediment is captured well, and experimental gas production, dynamic volumetric strain and pressure response were closely reproduced. In our simulations, Youngs modulus of the gas hydrate-bearing sediment is considered to be dependent on gas hydrate saturation. The individual Youngs moduli of gas hydrate-free sediment and pure gas hydrate were calibrated based on stress-strain behavior observed during periods of constant and known gas hydrate saturation. Differences of apparent stress-strain behavior during gas hydrate formation and dissociation periods indicate that the gas hydrate-sediment structure and bulk hydrate distribution were largely different during these periods, and composite Youngs modulus showed a much stronger dependency on bulk gas hydrate saturation during gas hydrate formation. Our results indicate that the understanding of gas hydrate-sediment fabrics and stress-strain behavior during dynamic gas hydrate formation and dissociation needs to be improved further.

KEYWORDS: Gas hydrate reservoir simulator; thermo-hydro-chemo-mechanical model; poro-elasticity; Youngs modulus; depressurization; natural gas production; triaxial test

INTRODUCTION

Methane gas hydrates are crystalline solids formed from water molecules enclathrating methane molecules. Methane hydrates are thermodynamically stable under conditions of low temperatures and high pressures and occur in nature in permafrost regions and the deep-sea. If warmed or depressurized, methane hydrates destabilize and dissociate into water and methane gas. Natural gas hydrates are considered to be a promising energy resource. It is widely believed that the energy content of methane occurring in hydrate form is immense, possibly exceeding the combined energy content of

all other conventional fossil fuels (Piñero *et al.* (2013), Burwicz *et al.* (2011), Archer *et al.* (2009), Milkov (2004), Kvenvolden (1993)).

Several methods have been proposed for production of natural gas from gas hydrate reservoirs through thermal stimulation, depressurization or chemical activation (Moridis *et al.* (2009, 2011), Park *et al.* (2006), Lee *et al.* (2003)). Currently, depressurization being the most mature approach, there is a strong focus on evaluating the potential for using depressurization as the essential driving force for releasing gas from natural gas hydrate reservoirs. Recent field trials, onshore below the Alaskan permafrost and in the Nankai Trough offshore Japan were essentially depressurization tests; the Japanese test used only depressurization (Yamamoto (2013, 2015), David (2013)), while, the Alaskan test was combined with $N_2 : CO_2$ injection (Anderson *et al.* (28 July - 1 August, 2014), Schoderbek *et al.* (October 1, 2008-June 30, 2013)).

Manuscript received...

* Chair for Numerical Mathematics, Technical University Munich, Boltzmannstraße 3, 85748 Garching bei München, Germany
Email: gupt@ma.tum.de (Shubhangi Gupta)

† GEOMAR Helmholtz Centre for Ocean Research Kiel, Wischhofstraße 1-3, D-24148 Kiel, Germany

Email: cdeusner@geomar.de (Christian Deusner)

‡ Dept. of Hydromechanics and Modelling of Hydrosystems, University of Stuttgart, Pfaffenwaldring 61, 70569 Stuttgart, Germany

Although sediment stability issues resulting from gas hydrate dissociation and fluid flow, e.g. soil consolidation, seafloor subsidence and wellbore integrity, were far from being unexpected according to earlier simulation studies (Ning *et al.* (2012), Rutqvist *et al.* (2009, 2012)), the nature and extent of the geotechnical problems observed during the field trials were beyond predictions, and sediment destabilization and sand production could not be sufficiently controlled. Because of these apparent process management and safety concerns, it is important to carefully evaluate future technologies for gas extraction from gas hydrate reservoirs and to include detailed risk quantification from inherent geohazards in the particular situation and setting.

Multiphysics models for strongly coupled hydro-thermo-chemo-geomechanical processes related to gas hydrates are becoming a powerful tool for making such performance evaluations (Gupta *et al.* (2015), M. *et al.* (2014), Rutqvist (2011), Klar *et al.* (2010)), although computing power necessary for detailed field scale modeling can be huge (Reagan *et al.* (2015)). The predictive value of such numerical models depends on their ability to capture the influence of important variables such as gas hydrate saturation and its distribution in relation to sediment characteristics, as well as to describe how this behavior changes when gas hydrate-soil fabrics are dynamically altered during and after gas production. Thus, to be able to make any predictions with confidence, the numerical models need to be thoroughly validated against experimental and field data.

Numerous experimental studies on mechanical behavior of gas hydrate-bearing sediments have been carried out in the past. Small-strain mechanical properties such as P - and S -wave velocities of gas hydrate-bearing soils with various soil types and gas hydrate saturations have been evaluated to calibrate geophysical field data, and to allow prediction of small strain strength and stiffness, volume yield behavior and subsidence upon changes in gas hydrate saturation and gas hydrate-soil fabrics under defined stress conditions (Winters *et al.* (2007), Lee *et al.* (2010a), Priest *et al.* (2005, 2009)). It is generally agreed on that the distribution of gas hydrates and the gas hydrate-soil skeleton has marked influence on strength and stiffness behavior, such that gas hydrates formed in gas-saturated soil increase stiffness and strength already at low gas hydrate saturations, whereas, pore filling gas hydrates formed in water-saturated soils only become effective at higher gas hydrate saturations ($\approx 0.4 - 0.5$) (Waite *et al.* (2009)). Material models were frequently obtained using THF to allow for fast and controlled gas hydrate formation in the laboratory without the necessity of having a free gas phase and more complicated volume change behavior (Lee *et al.* (2010a), Yun *et al.* (2007)). Large-strain deformation under deviatoric loading, and dynamic stress-strain behavior during depressurization or thermal stimulation was studied in triaxial experiments (Hyodo

et al. (2013); M. *et al.* (2014), Song *et al.* (2014), Ghiassian & Grozic (2013)). In the very recent past, there have also been the first attempts to carry out studies on undisturbed pressure cores, which will clearly advance the field towards a much better understanding of the mechanics of the gas hydrate-bearing soils (Inada & Yamamoto (2015), Santamarina *et al.* (2015), Yoneda *et al.* (2015)).

Experimental results and micro-mechanical considerations have led to the development of different mathematical formulations for elastic strain parameters (Young's modulus, Poisson ratio). For example, Sultan & Garziglia (2011) assume a linear relationship between gas hydrate stiffness and gas hydrate saturation, which is supported by experimental results reported by Soga *et al.* (2006) and Waite *et al.* (2009), while Miyazaki *et al.* (2010) relate gas hydrate stiffness and peak strength with the strain-rate, besides considering a non-linear relationship between the stiffness and the hydrate saturation. The formulation in this study is based on the earlier findings reported in Santamarina & Ruppel (2010), who propose that the effective-stress dependent soil stiffness and the gas-hydrate stiffness contribute additively to the stiffness of the gas-hydrate-bearing sediment. The stiffness contribution from gas hydrates is considered as varying non-linearly with the gas hydrate saturation and is, thus, much more pronounced at high gas hydrate saturations.

In this study, we combine high-pressure triaxial experimentation with coupled multiphysics simulation of methane hydrate formation and dissociation. We perform a controlled triaxial volumetric strain test on a sand sample in which methane hydrate is first formed under controlled effective stress and then dissociated via depressurization under controlled total stress. We assume that this is realistic for natural settings in which gas hydrates have been formed at increased hydrostatic pressure but in relatively shallow, unconsolidated sediments at low effective stress, and depressurization is carried out under drained conditions without changing the sediment and bulk fluid overburden, thus assuming gas hydrates being located in a highly permeable formation, which is confined by sediment regions of much lower permeability. Gas hydrate in our experiment was initially formed by pressurizing partially water-saturated sand with gaseous methane to reach a gas hydrate saturation of 0.4, and remaining methane gas was replaced with seawater before the sample was depressurized stepwise. Confining and axial loads in triaxial testing are applied isotropically and controlled in a suitable manner to keep the deformation of the sample small; shear loads are not applied. Under these constraints, we assume concepts of poro-elasticity to be essentially valid. We numerically simulate this test using the hydro-geomechanical hydrate reservoir code developed by Gupta *et al.* (2015). The focus of this manuscript is laid on testing how well the linear elastic model can capture the dynamic coupling between the transport, chemical reaction, and mechanical processes during methane

hydrate formation and dissociation in sandy soil under isotropic loading, and, further, to evaluate the suitability and further needs towards extension of our simulation approach to capture more complex elastic-plastic deformation scenarios and issues of sand production, as observed in the above mentioned field trials for gas production from natural gas hydrate reservoirs.

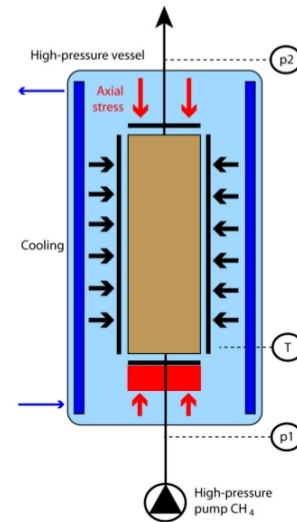
MATERIAL AND METHODS

Experimental set-up and components

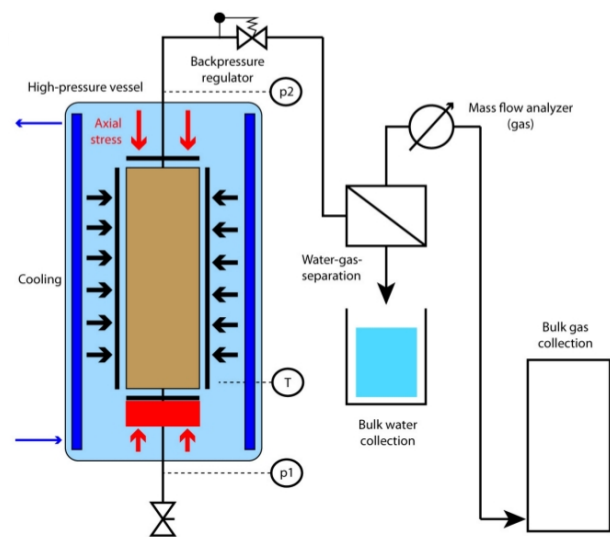
Experiments were carried out in the custom-made high pressure apparatus NESSI (Natural Environment Simulator for Sub-seafloor Interactions, Deusner *et al.* (2012)), which was equipped with a high-pressure triaxial cell mounted in a 40 L stainless steel vessel (APS GmbH Wille Geotechnik, Rosdorf, Germany). All wetted parts of the setup are made of stainless steel. Salt water medium was supplied from reservoir bottles (DURAN, Wertheim, Germany) using a HPLC pump S1122 (SYKAM, Frstenfeldbruck, Germany). Pressure was adjusted with a back-pressure regulator valve (TESCOM Europe, Selmsdorf, Germany). Experiments were carried out in upflow mode with injection of CH_4 gas and seawater medium at the bottom of the sample prior and after gas hydrate formation (Fig. 1a), and fluid discharge at the top of the sample during depressurization (Fig. 1b). Axial and confining stresses, and sample volume changes were monitored throughout the overall experimental period. Pore pressure was measured in the influent and the effluent fluid streams close to sample top and bottom. The experiment was carried out at constant temperature conditions. Temperature control was achieved with a thermostat system (T1200, Lauda, Lauda-Knigshofen, Germany). Produced gas mass flow was analyzed with mass flow controllers (EL FLOW, Bronkhorst, Kamen, Germany). For control purposes, bulk effluent fluids were also collected inside 100 L gas tight TEDLAR sampling bags (CEL Scientific, Santa Fe Springs CA, USA). The sampling bags were mounted inside water filled containers. After expansion of the effluent fluids at atmospheric pressure, overall volume was measured as volume of water displaced from these containers.

Sample preparation and mounting

The sediment sample was prepared from quartz sand (initial sample porosity: 0.35, grain size: 0.1 – 0.6 mm, G20TEAS, Schlingmeier, Schwülper, Germany), which was mixed with deionized water to achieve a final water saturation of 0.4 relative to initial sample porosity. The partially water saturated and thoroughly homogenized sediment was filled into the triaxial sample cell equipped with a Viton sleeve to obtain final sample dimensions of 380 mm in height and 80 mm in diameter. Sample geometry was assured using a sample forming device. The sample was cooled to $2^{\circ}C$ after the triaxial cell was mounted inside the pressure vessel. Initial water permeability of gas hydrate-free sediment was $5 \times 10^{-10} m^2$.



(a) Gas hydrate formation



(b) Depressurization and gas production

Fig. 1. Simplified flow schemes for relevant experimental periods

Experimental procedure

Gas hydrate formation

Prior to gas hydrate formation the sediment sample was isotropically consolidated to 2 MPa effective stress under drained conditions. The sample was flushed with CH_4 gas and, subsequently, pressurized with CH_4 gas to approximately 12.5 MPa (Fig. 1a). During pressurization with CH_4 gas and throughout the overall gas hydrate formation period, formation stress conditions of 2 MPa effective stress were maintained using an automated control algorithm. The formation process was continuously monitored by logging the CH_4 gas pressure. Mass balances and volume saturations were calculated based on CH_4 gas pressure and initial mass and volume values. Gas hydrate formation was terminated after 1.84 mol of CH_4 -hydrates had been formed after approximately 6 days, corresponding to CH_4 -hydrate saturation of 0.39. The sample was cooled to $-5^{\circ}C$ and stress control was switched to constant

total isotropic stress control at approximately 9 MPa before the sample pore space was de-pressurized to atmospheric pressure and remaining CH_4 gas in the pore space was released. System re-pressurization and water saturation of pore space was achieved by instant filling and re-pressurization with pre-cooled ($-1^{\circ}C$) saltwater medium according to seawater composition. Hydrate dissociation during the brief period of depressurization was minimized by taking advantage of the anomalous self-preservation effect, which reaches an optimum close to the chosen temperature (Stern *et al.* (2003)). After completion of gas - water fluid exchange, the sample temperature was re-adjusted to $2^{\circ}C$.

Depressurization and gas production

The sample pore space was de-pressurized and gas produced by stepwise decrease of back pressure at constant isotropic total stress (Fig.1b). Overall fluid production (water and CH_4 gas) was monitored after de-pressurization at ambient pressure after temperature equilibration.

NUMERICAL SIMULATION

To simulate the hydrate formation and dissociation processes in the lab-scale triaxial compression experiment described in Section , we use the mathematical model and the numerical simulator developed by S.Gupta *et al.* (2015). This model considers kinetic hydrate phase change and non-isothermal, multi-phase, multi-component flow through poro-elastic porous medium. The model accounts for the effect of hydrate phase change on the mechanical properties of the sediment, and also for the effect of sediment deformation on the fluid-solid interaction properties relevant to reaction and transport processes (e.g., reaction surface area, permeability, capillary pressure).

Mathematical model

The model considers three *components*: CH_4 , H_2O and methane hydrate ($CH_4 \cdot N_h (H_2O)$), which are present in three distinct *phases*: gaseous, aqueous, and solid. The gaseous phase comprises of methane gas and water vapour. The aqueous phase comprises of water and dissolved methane. The solid phase comprises of pure methane hydrate and sand grains. The sand grains are assumed to form a material continuum which provides the skeletal structure to the porous medium. We shall refer to this as *solid matrix*. The aqueous, gaseous, and hydrate phases exist in the void spaces of this solid matrix (See Fig.2). The hydrate is assumed to be of grain-coating type because it was formed from gas-saturated wet sand. It is further assumed that the hydrate sticks perfectly on the surface of the sand grains, such that the sand and hydrate together form a *composite solid matrix*. This assumption allows us to write a single momentum balance equation for the composite-solid, instead of separate ones for sand and hydrate phases each.

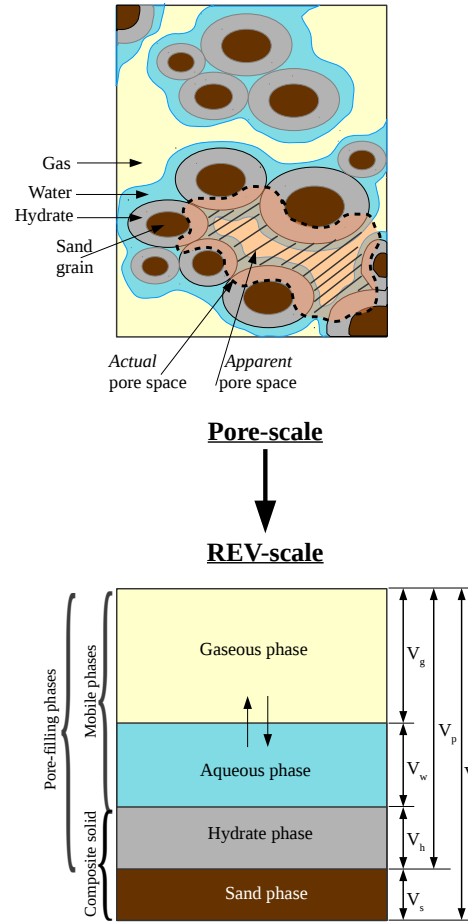


Fig. 2. Pore-scale to REV-scale

A summary of the governing equations and the constitutive relationships is given in Table 1. The phases occupying the pore space (gaseous, aqueous, hydrate) are denoted by ' β ' = g, w, h respectively, the mobile phases (gaseous and aqueous) are denoted by ' α ' = g, w , and the mobile molecular components are denoted by ' κ ' = CH_4, H_2O . The solid matrix is designated with the subscript ' s '. The sand+hydrate composite solid matrix is designated with the subscript ' sh '. ' γ ' is used to denote all phases, i.e., $\gamma = g, w, h, \text{ and } s$.

Primary variables

The mathematical model consists of the following 6 governing equations: the mass balance Eqns. (1,2,3,4), the momentum balance Eqn. (7) for the composite-solid, and the energy balance Eqn. (8). The momentum balance Eqns. (5,6) for the mobile phases $\alpha = g, w$ give the α -phase velocities directly, and are thus absorbed in the mass and energy balance equations. We chose the following set of variables as the primary variables: the gas phase pressure P_g , the aqueous phase saturation S_w , the hydrate phase saturation S_h , the temperature T , the total-porosity ϕ , and, the composite-matrix displacement \mathbf{u} . All other variables can be derived (explicitly or implicitly) from this set of variables using the closure and constitutive relationships.

Table 1. Summary of the mathematical model

Governing equations		eqn. no.
Mass balance for each mobile component $\kappa = CH_4, H_2O$	$\sum_{\alpha} [\partial_t (\phi \rho_{\alpha} \chi_{\alpha}^{\kappa} S_{\alpha})] + \sum_{\alpha} [\nabla \cdot (\phi \rho_{\alpha} \chi_{\alpha}^{\kappa} S_{\alpha} \mathbf{v}_{\alpha,t})] = \sum_{\alpha} [\nabla \cdot (\phi S_{\alpha} \mathbf{J}_{\alpha}^{\kappa})] + \dot{g}^{\kappa} + \sum_{\alpha} \dot{q}_{m_{\alpha}}^{\kappa} + \dot{S}_{ext}^{\kappa}$	(1),(2)
Mass balance for hydrate phase	$\partial_t (\phi \rho_h S_h) + \nabla \cdot (\phi \rho_h S_h \mathbf{v}_{h,t}) = \dot{g}^h$	(3)
Mass balance for sand phase	$\partial_t [(1 - \phi) \rho_s] + \nabla \cdot ((1 - \phi) \rho_s \mathbf{v}_s) = 0$	(4)
Momentum balance for mobile phases $\alpha = g, w$	$\mathbf{v}_{\alpha} = -K \frac{k_{r\alpha}}{\mu_{\alpha}} (\nabla P_{\alpha} - \rho_{\alpha} \mathbf{g}) \quad \text{(Darcy's Law)}$	(5),(6)
Momentum balance for composite - solid	$\nabla \cdot \tilde{\sigma} + \rho_m \mathbf{g} = 0$ where, ρ_m is the bulk density given by $\rho_m = \sum_{\beta} (\phi S_{\beta} \rho_{\beta}) + (1 - \phi) \rho_s$	(7)
Energy balance	$\partial_t \left[(1 - \phi) \rho_s u_s + \sum_{\beta} (\phi S_{\beta} \rho_{\beta} u_{\beta}) \right] + \sum_{\alpha} [\nabla \cdot (\phi \rho_{\alpha} \chi_{\alpha}^{\kappa} S_{\alpha} \mathbf{v}_{\alpha,t} h_{\alpha})] = \nabla \cdot k_{eff}^c \nabla T + \dot{Q}_h + \sum_{\alpha} (\dot{q}_{m_{\alpha}}^{\kappa} h_{\alpha})$ where, $k_{eff}^c = (1 - \phi) k_s^c + \sum_{\alpha} \sum_{\kappa} (\phi \chi_{\alpha}^{\kappa} S_{\alpha} k_{\alpha}^c) + \phi S_h k_h^c$ $h_{\alpha} = \int_{T_{ref}}^T C p_{\alpha} dT$ $u_{\gamma} = \int_{T_{ref}}^T C v_{\gamma} dT$	(8)
Closure relationships		
Relationship between phase pressures	$P_g - P_w = P_c (S_{we})$	(9)
Summation relationships	$\sum_{\beta} S_{\beta} = 1$ $\sum_{\kappa} \chi_{\alpha}^{\kappa} = 1$	(10) (11),(12)

Constitutive relationships**1. Vapor-liquid equilibrium**

Using Henry's Law and Raoult's Law for ideal gas - liquid solutions,

For dissolved methane: $\chi_w^{CH_4} = H(T) \chi_g^{CH_4} P_g$

For water vapor: $\chi_g^{H_2O} = \chi_w^{H_2O} \frac{P_{H_2O}^{sat}(T)}{P_g}$

where, $H(T)$ is the Henry's constant for methane dissolved in water calculated using the empirical relation from NIST database ([Sander \(retrieved February 23, 2015\)](#)), and $P_{H_2O}^{sat}$ is saturated water vapour pressure calculated using Antoine's equation.

2. Diffusive mass-transfer flux

Fick's law: $\mathbf{J}_{\alpha}^{\kappa} = -\tau D^{\alpha} (\rho_{\alpha} \nabla \chi_{\alpha}^{\kappa})$

where, D^{α} is the binary diffusion coefficient.

D^g is estimated using the empirical relationship proposed by [Statterly & Bird \(June 1958\)](#) for low density binary CH_4H_2O system.

D^w is estimated using the Wilke-Chang correlation ([Himmelblau \(1964\)](#)) for dilute associated liquid mixtures is used.

Continued on next page

Table 1 – Summary of the mathematical model (*continued*)

eqn. no.

3. Hydrate phase change kinetics

Non-equilibrium phase change of methane hydrate is modeled by the Kim-Bishnoi kinetic model (Kim *et al.* (1987)).

$$\text{Gas generation rate} \quad \dot{g}^{CH_4} = k_{reac} M_{CH_4} A_{rs} (P_e - f_g) \quad (13)$$

where,

k_{reac} is the rate of kinetic phase-change,

P_e is the hydrate equilibrium pressure, modelled as (Kamath (1984)),

$$P_e = A_1 \exp \left(A_2 - \frac{A_3}{T} \right), \quad (14)$$

f_g is the gas fugacity calculated using the Peng-Robinson EoS for methane gas, and,

A_{rs} is the specific reaction surface area modelled as $A_{rs} = \Gamma_r A_s$, where,

A_s is the total surface area and Γ_r is the ratio of the active reaction surface

to the total surface area. A_s and Γ_r are modelled using the correlations

proposed by Yousif (1991) and Sun & Mohanty (2006), respectively,

leading to,

$$A_{rs} = \begin{cases} \phi S_h \sqrt{\frac{\phi_{eff}^3}{2K}} & , \text{ if } (P_e - f_g) \geq 0 \\ (S_g S_w S_h)^{\frac{2}{3}} \sqrt{\frac{\phi_{eff}^3}{2K}} & , \text{ if } (P_e - f_g) < 0 \end{cases} \quad (15)$$

$$\text{Water generation rate} \quad \dot{g}^{H_2O} = \dot{g}^{CH_4} N_{Hyd} \frac{M_{H_2O}}{M_{CH_4}} \quad (16)$$

$$\text{Hydrate consumption rate} \quad -\dot{g}^{Hyd} = \dot{g}^{CH_4} \frac{M_{Hyd}}{M_{CH_4}} \quad (17)$$

$$\text{Heat of hydrate dissociation} \quad \dot{Q}_h = \frac{-\dot{g}^{Hyd}}{M_{Hyd}} \left(B_1 - \frac{B_2}{T} \right) \quad (18)$$

4. Properties of the fluid-matrix interaction

$$\text{Capillary pressure} \quad P_c = P_{c0} \cdot f_{S_h}^{P_c}(S_h) \cdot f_{\phi}^{P_c}(\phi) \quad (19)$$

where,

P_{c0} is capillary pressure for un-deformed, un-hydrated solid matrix, given by Brooks-Corey relationship,

$$P_{c0} = P_{entry} S_{we}^{-1/\lambda_{BC}}, \quad (20)$$

and, $f_{S_h}^{P_c}(S_h)$ and $f_{\phi}^{P_c}(\phi)$ are scaling factors to account for the effects of S_h (Rockhold *et al.* (2002)) and ϕ (Civan's power-law correlation Civan (2000)) respectively,

$$f_{S_h}^{P_c} = (1 - S_h)^{-\frac{3\lambda_{BC}-1}{3\lambda_{BC}}} \quad \text{and} \quad f_{\phi}^{P_c} = \frac{\phi_0}{\phi} \left(\frac{1 - \phi}{1 - \phi_0} \right)^2 \quad (21)$$

$$\text{Intrinsic permeability} \quad K = K_0 \cdot f_{S_h}^K(S_h) \cdot f_{\phi}^K(\phi) \quad (22)$$

where,

K_0 is intrinsic permeability of the un-deformed, un-hydrated solid matrix,

and, $f_{S_h}^K(S_h)$ and $f_{\phi}^K(\phi)$ are scaling factors to account for the effects of

S_h (Rockhold *et al.* (2002)) and ϕ (Civan (2000)) respectively,

$$f_{S_h}^K = (1 - S_h)^{\frac{19}{6}} \quad \text{and} \quad f_{\phi}^K = \frac{\phi}{\phi_0} \left(f_{\phi}^{P_c} \right)^{-2} \quad (23)$$

Relative permeabilities

Relative permeabilities of the mobile phases are modelled using

Brooks-Corey model in conjunction with the Burdine theorem (Burdine (1953)), as

$$k_{rw} = S_{we}^{\frac{2+3\lambda_{BC}}{\lambda_{BC}}} \quad \text{and} \quad k_{rg} = (1 - S_{we})^2 \left(1 - S_{we}^{\frac{2+\lambda_{BC}}{\lambda_{BC}}} \right) \quad \text{where,} \quad (24)$$

$$S_{we} = \frac{S_w}{1 - S_h}$$

Continued on next page

Table 1 – Summary of the mathematical model (*continued*)

		eqn. no.
Hydraulic tortuosity	$\tau = \phi^n$ where, $1 \leq n \leq 3$	(25)
5. Poro-elasticity		
Effective stress principle	Effective stress concept introduced by Terzaghi (1925) and modified by Biot (1941) is used. $\tilde{\sigma} = \tilde{\sigma}' + \alpha_{biot} \left(\frac{S_g P_g + S_w P_w}{S_g + S_w} \right) \tilde{I}$ where, $\tilde{\sigma}$ is the total stress acting on the bulk porous medium, and $\tilde{\sigma}'$ is the effective stress acting on the composite skeleton. α_{biot} is the Biot-Willis constant (Biot & Willis (1957)).	(26)
Linear elastic stress-strain law	$\tilde{\sigma}' = 2 G_{sh} \tilde{\epsilon} + \lambda_{sh} (tr \tilde{\epsilon}) \tilde{I}$ where, $\tilde{\epsilon}$ is the linearized strain, given by $\tilde{\epsilon} = \frac{1}{2} (\nabla \mathbf{u} + \nabla^T \mathbf{u})$ and, G_{sh} and λ_{sh} are the Lamé's parameters. In terms of Young's modulus E_{sh} , and Poisson's ratio ν_{sh} , $G_{sh} = \frac{E_{sh}}{2(1 + \nu_{sh})}, \lambda_{sh} = \frac{E_{sh} \nu_{sh}}{(1 + \nu_{sh})(1 - 2\nu_{sh})}$	(27) (28) (29)
Young's modulus	Young's modulus E_{sh} is modelled using the parameterization proposed by Santamarina & Ruppel (2010) . $E_{sh} = E_s + S_h^c E_h$ where, E_s and E_h can be interpreted as the Young's modulus of hydrate-free sand and hydrate, respectively. The effect of confining stresses on the solid skeleton are implicit in the definition of E_s .	(30)

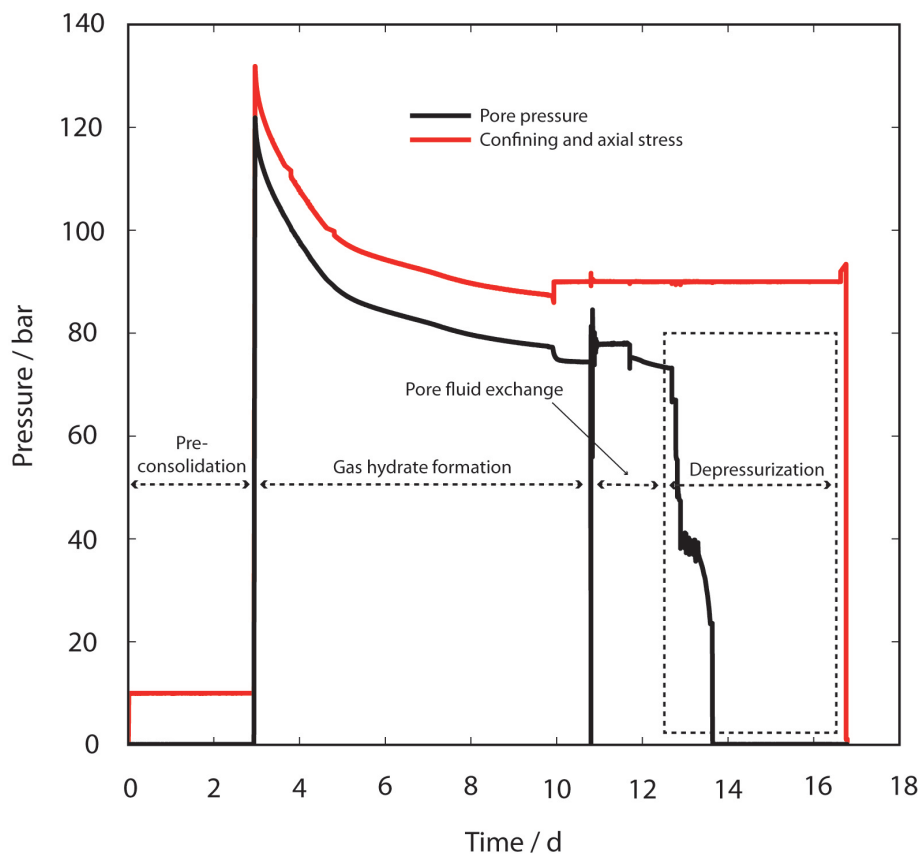
Table 2. Material properties and model parameters

			Ref.
Thermal conductivities			
k_g^c	$-0.886 \times 10^{-2} + 0.242 \times 10^{-3}T - 0.699 \times 10^{-6}T^2 + 0.122 \times 10^{-8}T^3$	$W \cdot m^{-1} \cdot K^{-1}$	Roder (1985)
k_w^c	$0.3834 \ln(T) - 1.581$	$W \cdot m^{-1} \cdot K^{-1}$	IAP (2008)
k_h^c	2.1	$W \cdot m^{-1} \cdot K^{-1}$	Sloan & Koh (2007)
k_s^c	1.9	$W \cdot m^{-1} \cdot K^{-1}$	Esmailzadeh et al. (2008)
Specific heat capacities			
Cp_g	$\Delta Cp_g^{res} (1238 + 3.13T + 7.9 \times 10^{-4}T^2 - 6.86 \times 10^{-7}T^3)$	$J \cdot kg^{-1} \cdot K^{-1}$	Peng & Robinson (1976); Esmailzadeh et al. (2008)
Cv_g	$Cp_g + R_{CH_4}$	$J \cdot kg^{-1} \cdot K^{-1}$	
Cp_w	4186	$J \cdot kg^{-1} \cdot K^{-1}$	IAP (2008)
Cv_w	$Cp_w + R_{H_2O}$	$J \cdot kg^{-1} \cdot K^{-1}$	
Cv_h	2700	$J \cdot kg^{-1} \cdot K^{-1}$	Sloan & Koh (2007)
Cv_s	800	$J \cdot kg^{-1} \cdot K^{-1}$	Esmailzadeh et al. (2008)
Dynamic viscosities			
μ_g	$10.4 \times 10^{-6} \left(\frac{273.15 + 162}{T + 162} \right) \left(\frac{T}{273.15} \right)^{1.5}$	$Pa \cdot s$	Friend et al. (1989)
μ_w	$0.001792 \exp \left[-1.94 - 4.80 \left(\frac{273.15}{T} \right) + 6.74 \left(\frac{273.15}{T} \right)^2 \right]$	$Pa \cdot s$	IAP (2008)
Densities			
ρ_g	$\frac{P_g}{zR_gT}$	$kg \cdot m^{-3}$	Peng & Robinson (1976)

Continued on next page

Table 2 – Material properties and model parameters (*continued*)

ρ_w	vapour: $0.0022 \frac{P_g}{T}$	$kg \cdot m^{-3}$	IAP (2008)
	liquid: 1000	$kg \cdot m^{-3}$	IAP (2008)
ρ_h	900	$kg \cdot m^{-3}$	Sloan & Koh (2007)
ρ_s	2100	$kg \cdot m^{-3}$	
Hydraulic properties			
λ_{BC}	1.2		Helmig (1997)
P_{entry}	50	kPa	Helmig (1997)
Hydrate kinetics			
k_{rea}	formation: 0.2×10^{-11}	$mol \cdot m^{-2}$	
	dissociation: 3.2×10^{-10}	$Pa^{-1} \cdot s^{-1}$	
N_{Hyd}	5.75		
$P_{e,0}$	$A_1 = 10^6, A_2 = 38.98, A_3 = 8533.8$	Pa	Kamath & Holder (1987)
\dot{Q}_h	$B_1 = 56599, B_2 = 16.744$	$W \cdot m^{-3}$	Esmailzadeh <i>et al.</i> (2008)
Poroelasticity parameters			
α_{biot}	0.8		Verruijt (2008)
ν_{sh}	0.15		Miyazaki <i>et al.</i> (2011)
	formation	dissociation	
E_s	1032	160	MPa
E_h	250	360	MPa
c	1	3	

Fig. 3. Overview of the *measured* pressure and stresses over time.

Solution strategy

We use an iteratively coupled solution strategy. The mathematical model is decoupled into three parts:

1. flow/transport subsystem (\mathbf{F}_f), comprised of the mass balance equations for CH_4 , H_2O , and Hydrate, and the energy balance equation,
2. geomechanical subsystem (\mathbf{F}_g), comprised of the momentum balance equation for composite solid phase, and
3. porosity equation (\mathbf{F}_ϕ), comprised of the mass balance equation for the sand phase.

\mathbf{F}_f is solved for the variables P_g , S_w , S_h , and T , \mathbf{F}_g is solved for displacements \mathbf{u} , and \mathbf{F}_ϕ is solved for total porosity ϕ . \mathbf{F}_f and \mathbf{F}_ϕ are spatially discretized using a fully upwinded cell centered finite volume method. Orthogonal grids aligned with the principal axes are defined and a control-volume formulation with two-point flux approximation (TPFA) is used. \mathbf{F}_g is discretized using Galerkin finite element (FEM) method defined on $Q1$ elements. An implicit Euler time-stepping scheme is used for marching forward in time. The solution for a given time step involves two iterative loops, the *inner loop* and the *outer loop*. The *inner loop* uses Newton's method and SuperLU (Demmel *et al.* (September 1999)) linear solver to solve each of \mathbf{F}_f , \mathbf{F}_g , and \mathbf{F}_ϕ , thus taking care of the decoupled solution. The *outer loop* re-introduces the coupling between \mathbf{F}_f , \mathbf{F}_g , and \mathbf{F}_ϕ through a block Gauss Seidel iterative scheme.

The numerical scheme is implemented in the C++ based DUNE-PDELab framework (Dedner *et al.* (2012)), and is capable of solving problems in 1D, 2D and 3D domains.

Computational domain and test-setting

Assuming that the sand sample is axially symmetric, a 2D radial plane of dimensions 360 mm \times 40 mm is chosen as the computational domain. The dimensions correspond to the physical size of the sample. The domain is discretized into 72 \times 8 cells.

The overall experiment was carried out in four steps, viz. 1) *pre-consolidation*, 2) *gas hydrate formation*, 3) *pore-fluid exchange*, and 4) *depressurization*, as described in section . During steps 1 and 2, the sample was maintained under a defined effective loading with the confining and the axial stresses controlled to remain 10 bar above the pore pressure. However, during steps 3 and 4, the total isotropic stress was controlled to remain at a constant level. (See Fig. 3.) The experiment was performed over a total period of about 16.8 days. The *periods of interest* for the simulation are: 1) from *Day* – 3 to *Day* – 10, corresponding to gas hydrate formation, and 2) from *Day* – 12.8 to *Day* – 13.8, corresponding to

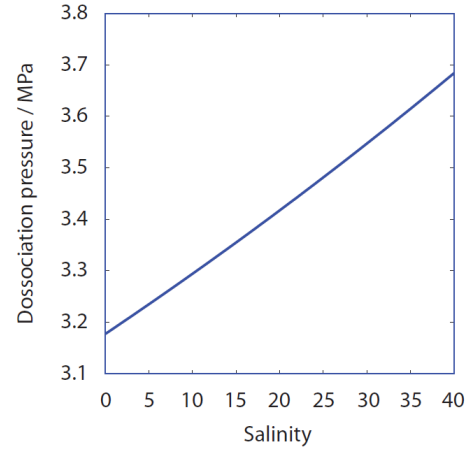


Fig. 6. Effect of salinity on hydrate stability curve (at $T_{bath} = 20^\circ C$)

depressurization and gas production. We simulate both of these periods separately.

Gas hydrate formation period: The schematic of the hydrate formation test is shown in Fig.4. The schematic also shows the initial and boundary conditions. The simulation is run until $t_{end} = 604800$ s (i.e. 7 days) using a maximum time step size of 120 s.

Depressurization and gas production period: The schematic of the depressurization test is shown in Fig.5. The schematic also shows the initial and boundary conditions. The simulation is run until $t_{end} = 86400$ s (i.e. 1 day) using a maximum time step size of 120 s.

The important material properties and model parameters are listed in Table 2. The values of the thermal conductivities, specific heat capacities, dynamic viscosities, and densities for each phase are chosen from standard literature, the references to which are included in the table. The Brooks-Corey parameters are chosen from the range of typically expected values for sand samples. The most important properties/parameters relevant to the simulation of the experimental data arise from 1) the hydrate-phase-change kinetics, and 2) the poro-elastic behaviour of the hydrate bearing sediments.

The hydrate phase-change is modelled by Eqns. (13,16-18). The hydrate-phase equilibrium pressure P_e in Eqn. (13) is modelled in accordance with the findings of Kamath (1984). For hydrates in pure water, the equilibrium pressure depends only on the temperature. However, for hydrates in sea water (which is the case for our sample), the equilibrium pressure also depends on the salinity, as shown in Fig.6. We account for effect of salinity on the hydrate equilibrium pressure through linear curve fitting on dissociation pressure vs. salinity curve of Fig.6, as,

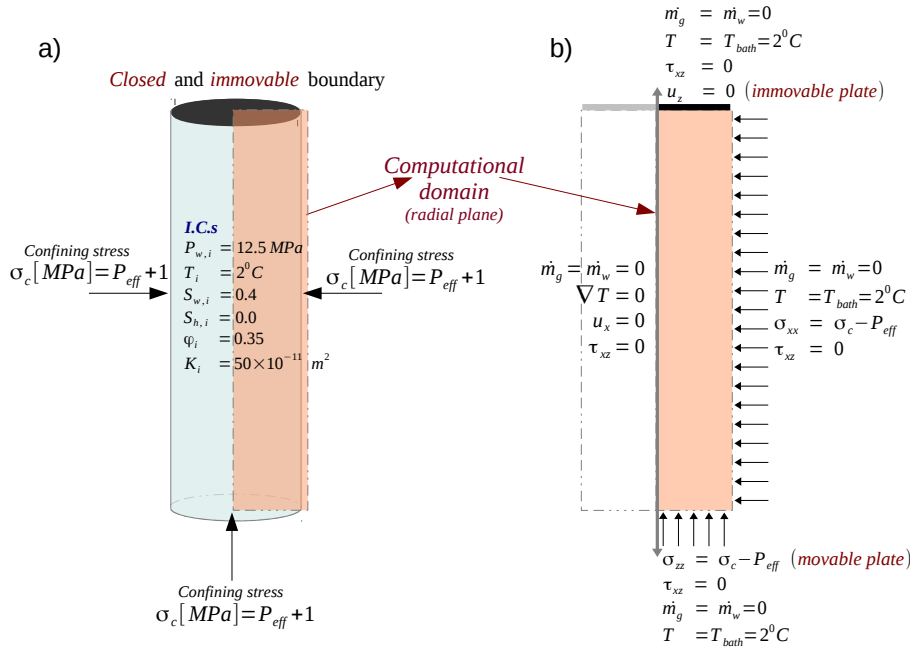


Fig. 4. Test setting for the gas hydrate formation period. a) shows the sample and the initial conditions, and b) shows the 2D computational domain and the boundary conditions.

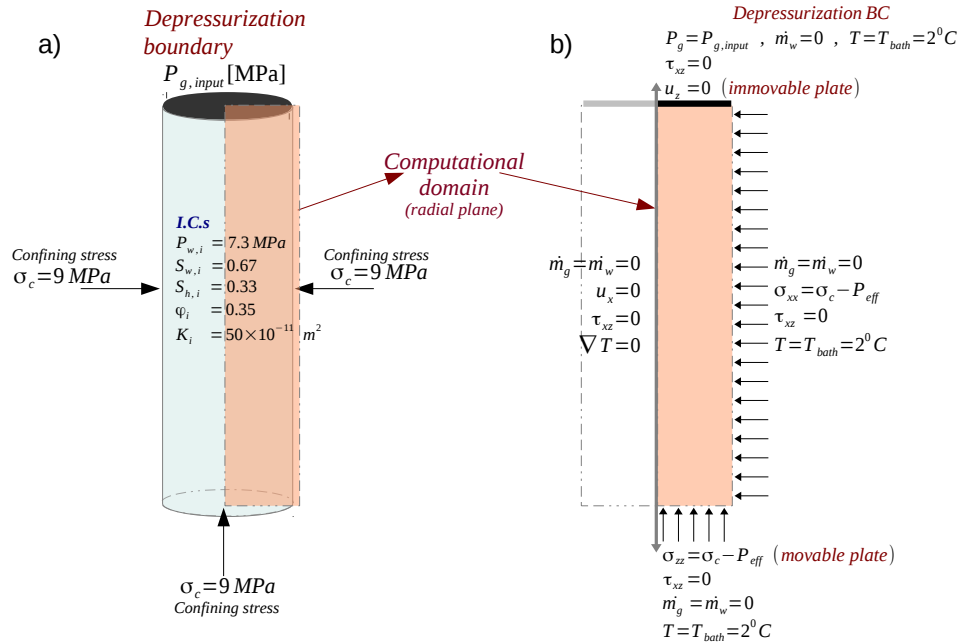


Fig. 5. Test setting for the depressurization and gas production period. a) shows the sample and the initial conditions, and b) shows the 2D computational domain and the boundary conditions.

$$P_e [\text{MPa}] = P_{e,0} - 0.5 + \frac{0.5}{40} s^0, \quad (31)$$

where, $P_{e,0}$ is hydrate stability curve for pure water with no salinity given by Eqn. (14), s_i^0 is the initial salinity of the sea-water in our sample, i.e., $s_i^0 = 35$, and s^0 is the salinity of the sea-water in the sample after dilution as a result of production of pure water from the dissociation of hydrate. Salinity s^0 at any given time is derived using the following argument: The

production of pure water reduces the salinity of the sea water in the sample. Assuming perfect mixing, for x amount of salt dissolved in the sea water,

$$x = s_i^0 V_{wi} = s^0 (V_{wi} + \Delta V_w)$$

where, V_{wi} is the initial volume of water in the sample, and ΔV_w is the volume of water produced due to hydrate

dissociation. Using the hydrate kinetics and rearranging, we get the expression for salinity s^0 as,

$$s^0 = s_i^0 \left[1 + N_h \frac{\rho_h M_w}{\rho_w M_h} \left(\frac{S_{h_i} - S_h}{S_{w_i}} \right) \right]^{-1}$$

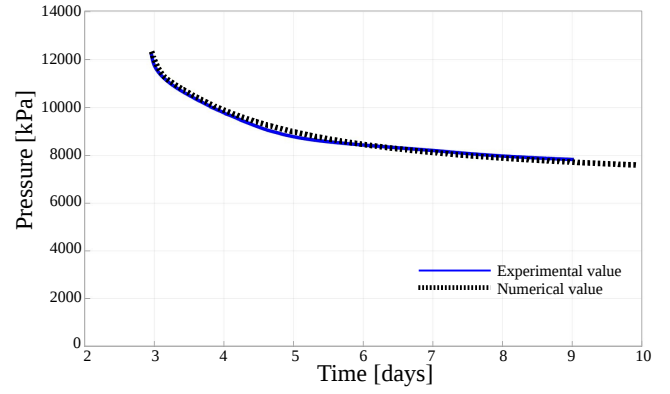
The reaction surface area, A_{rs} , in Eqn. (13), describes the surface area available for the kinetic-reaction, and puts a limit on the mass transfer during hydrate formation and dissociation. As the hydrate saturation in the pore-space increases, the availability of free surface for the hydrate formation to occur decreases, and vice versa. Additionally, for hydrate formation to occur, availability of both gas and water in sufficient quantities in the pore-space is a necessary condition. This behaviour of A_{rs} is modelled using the parameterization proposed by Sun & Mohanty (2006), given by Eqn. (15). The rate of reaction, k_{reac} , is a *free parameter* in our simulation which is used to calibrate the hydrate-kinetics model with respect to the experimental data. In the table we can see that the values of k_{reac} , for both hydrate formation as well as dissociation periods, lie well within the range reported in the literature.

The poro-elastic behaviour of the hydrate-bearing sediment is characterized by three parameters, viz., Biot's constant α_{biot} , Poisson ratio ν_{sh} , and Young's modulus E_{sh} . Biot's constant is chosen from a range of typically expected values. The Poisson's ratio is assumed to be a constant independent of the hydrate saturation following the experimental studies by Miyazaki *et al.* (2011). The Young's modulus is modelled using the parameterization proposed by Santamarina & Ruppel (2010), given by Eqn. (30). The Young's moduli E_s and E_h are *free parameters* which are used to calibrate the poro-elasticity model with respect to the experimental data. The choice of the exponent c is described in more detail in Section .

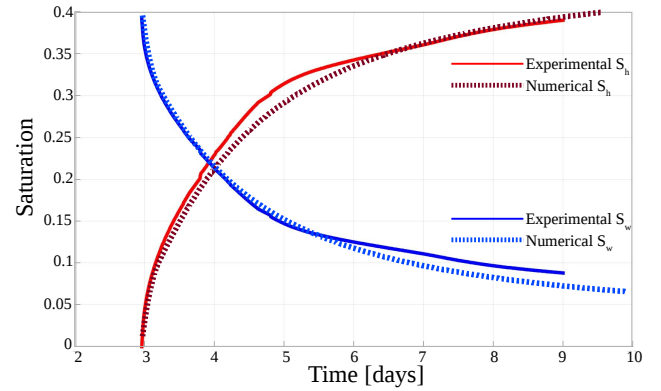
Simulation results

As discussed in Sec. , we essentially chose *one* free parameter in kinetics, i.e., k_{reac} , and *one* free parameter in linear-elasticity, which is E_{sh} , to calibrate the kinetics and the mechanical models separately. With these calibrated models, we simulate numerically the coupled hydro-mechanical response of the sand sample in triaxial test-setting using our gas hydrate reservoir model. The numerical results, together with the corresponding experimental data, are plotted in Fig. 7 for the gas hydrate formation period, and in Fig. 8 for the hydrate dissociation period.

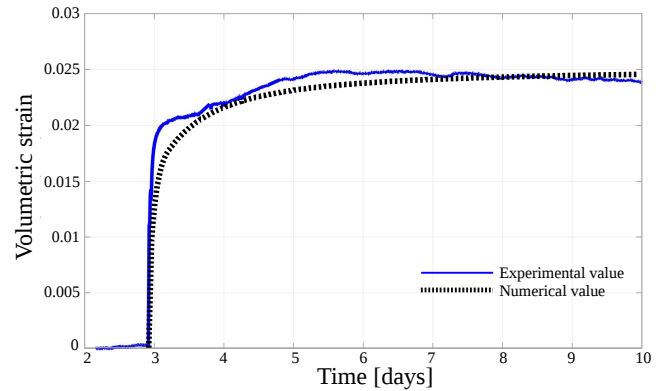
In the gas hydrate formation period, methane gas in the free pore space is continuously consumed and average bulk gas pressure is decreased. (See Fig. 7a. The experimental gas pressure is influenced by additional free volume space in inflow / outflow pipelines, which is considered in calculation and



(a) Average P_g in the domain over time



(b) Average S_w and S_h in the domain over time



(c) Total volumetric strain in the sample over time

Fig. 7. Comparison of the simulation results with the experimental results for the gas hydrate formation period.

simulation of saturations. See Appendix.) Clearly, the rate of gas hydrate formation is not constant. In the beginning, after the sample is pressurized at constant isotropic effective stress, gas hydrate formation from free methane gas and pore water is fast, but the rate of formation steadily decreases due to mass transfer limitations and shrinking reaction surfaces. In accordance to that, after pressurization the gas hydrate saturation increases rapidly and the water saturation decreases proportionally (Fig. 7b). The volumetric strain at constant effective stress shows a fast positive response during early gas hydrate formation

at relatively low gas hydrate saturation, and sample stiffness increases at higher gas hydrate saturation (Fig. 7c).

During the gas hydrate dissociation period, pressure is decreased step-wise until methane hydrates become unstable at the respective P-/T-conditions. Fig. 8a shows the numerically computed gas phase pressure in the sample. The gas production is plotted in Fig. 8b. With the onset of gas hydrate dissociation after reaching the hydrate stability boundary, pressure is maintained at a relatively constant level because hydrate dissociation and gas production equilibrate dependent on experimental and technical conditions.

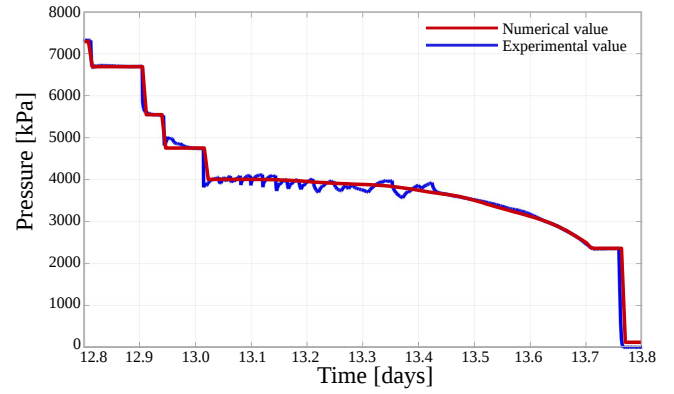
Volumetric strain during gas hydrate dissociation, plotted in Fig. 8c, is dependent on effective stress and gas hydrate saturation through the sample stiffness, which decreases with the ongoing gas hydrate dissociation and gas production.

Fig. 8d shows the numerically computed temperature profile of the sample during dissociation. The model predicts that sub-cooling from gas hydrate dissociation occurs, but is negligibly small on the sample scale due to isothermal temperature control.

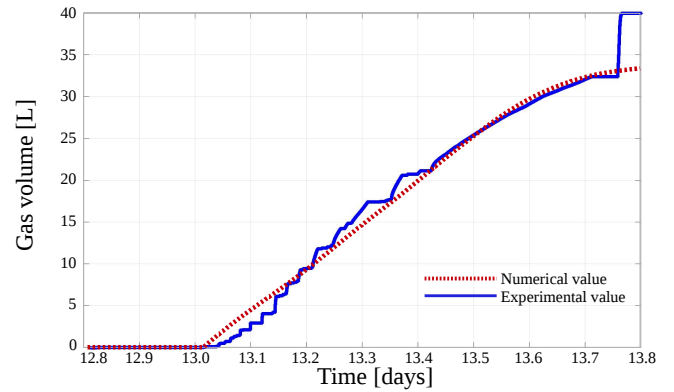
DISCUSSION AND OUTLOOK

From the results presented above, we can see that the developed model is capable of reproducing the dynamic thermo-hydro-chemo-mechanical behavior of methane hydrate-bearing sandy sediments. The key behaviors include gas hydrate formation and gas production rates and yields, pressure and temperature response, and bulk volumetric yielding observed in our triaxial compression experiments during gas hydrate formation in partially water-saturated sediment, as well as hydrate dissociation via depressurization.

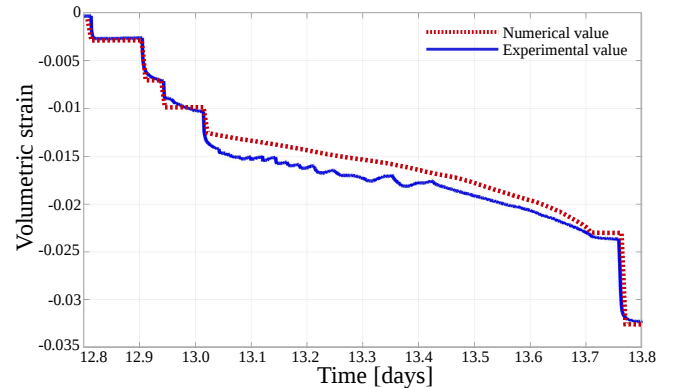
Overall, the experimental and simulation results on stress-strain behavior and elastic properties of gas hydrate-bearing sands are in accordance with earlier experimental and numerical studies, which reported Young's modulus or secant stiffness in a wide range of approximately 100 to 400 MPa for relevant gas hydrate concentrations (Brugada *et al.* (2010), Miyazaki *et al.* (2010), Lee *et al.* (2010b), Yun *et al.* (2007)). Stiffness measured in the presence of THF hydrates appears to be higher than for CH_4 -hydrates in sediments. Young's modulus in our simulations tends to relatively low values compared to the published experimental and numerical data, and approaches values for dense soils. This limited absolute contribution of gas hydrates to overall stiffness might be due to different sample preparation and consolidation schemes, relatively low gas hydrate saturations, or due to using CH_4 instead of THF, which was frequently used in published studies. It was recently concluded that CH_4 -hydrate in soils does not reveal soil-cementing capabilities (Chaouachi *et al.* (2015)),



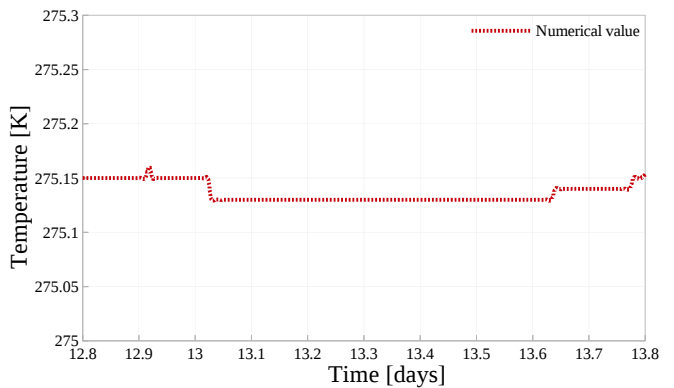
(a) P_g at depressurization boundary (at $z = 0$)



(b) Cumulative gas production over time



(c) Total volumetric strain in the sample over time



(d) Temperature in the sample over time

Fig. 8. Comparison of the simulation results with the experimental results for the depressurization and gas production period.

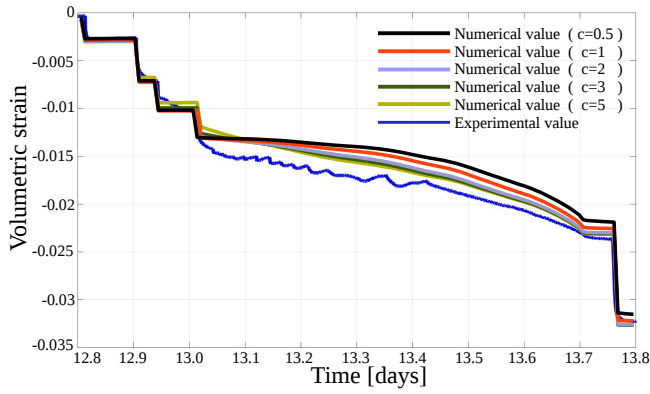


Fig. 9. Volumetric strain curves for different functional dependences of E_{sh} on S_h (i.e. $c = 1, 2, 3, 5$) for the depressurization and gas production period.

thus sediment stiffness can be expected to remain relatively unaffected at low gas hydrate saturations. However, this stress-strain behavior might also reflect differences in gas hydrate distribution and gas hydrate-soil fabrics. This aspect needs further evaluation in upcoming studies. We used a simple approach to describe composite Young's modulus E_{sh} , as being dependent on additive contributions of sand stiffness and gas hydrate stiffness, respectively. We have not included a contribution of effective stress conditions on the stiffness of gas hydrate-bearing sediment. Instead, we assume that during gas hydrate formation the effective stress is essentially constant, and during gas hydrate dissociation the stiffness of the sand is dominated by over-consolidation during gas-water exchange. Thus, effective stress effects on stiffness were assumed to be captured by adjusting Young's modulus of the soil matrix during gas hydrate formation and dissociation, respectively. Although the Young's modulus was treated as a free fitting parameter and initialized based on apparent stress-strain behavior during intervals of known and constant gas hydrate saturations, physically meaningful values for individual moduli E_s and E_h were obtained. The Young's modulus E_s for the sediment without gas hydrate reflected stiffness behavior typical for loose soil during gas hydrate formation while the sample was normally consolidated at low effective stress. In contrast, during the period of gas hydrate dissociation, gas hydrate-free sediment behaved like dense soil. This apparent step-like change of E_{sh} from 132 MPa to 183 MPa between gas hydrate formation and depressurization periods was presumably caused by over-consolidation during gas-water exchange at the end of the gas hydrate formation period. Thus, the gas hydrate-sand composite became stiffer without formation of additional gas hydrate.

The composite modulus E_{sh} depends almost linearly on S_h during gas hydrate formation, while during the hydrate dissociation period the dependence of E_{sh} on S_h is smaller. Fig. 9 shows the volumetric-strain plotted over time for the depressurization period for different functional dependences

of E_{sh} on S_h (i.e. $c = 0.5; 1; 2; 3; 5$). Our simulation results indicate that an exponent $c = 3$ is a reasonable approximation. Santamarina & Ruppel (2010) suggest that S_h tends to be raised to a power larger than 1, which reduces the impact on stiffness at low gas hydrate saturations relative to that for high gas hydrate saturations. Since we expect that gas hydrates formed in our procedure are predominantly located in the pore throats rather than in the free pore space, the linear and relatively strong dependence of E_{sh} on S_h appears reasonable. Under the initial conditions of only partial water saturation of the soil, the formed CH_4 -hydrate is assumed to contribute to the stiffness of the soil skeleton even at low gas hydrate saturations. This effect is further enhanced in weakly consolidated sediments, in which stiffness of the soil itself is low. The weak dependence of E_{sh} on gas hydrate saturation during dissociation appears also reasonable, since after exchanging gas with water in the pore space, gas hydrate-sediment fabrics will be steadily altered, and also during dissociation the grain-scale hydrate-sand structure is presumably changed. The mechanical implications of these structural transitions in gas hydrate-bearing sands during gas hydrate aging and dissociation are important issues. Any prediction of such dynamic changes in gas hydrate structure or its transient effects on geomechanics is yet not explicitly accounted for in our model, and needs further investigation.

For this experiment we have also ignored the effects of pore pressure and confining stresses on E_{sh} and other elastic material properties of the composite matrix. We have assumed that mechanical behavior of gas hydrate-bearing sands is dominated by gas hydrate saturation and effective stress conditions rather than by pore or cell pressure which is in accordance to earlier findings (Miyazaki *et al.* (2011)). However, contrasting results showing strengthening effects of high pore or confining pressures have also been reported (Song *et al.* (2014), Hyodo *et al.* (2013)).

Poisson ratio is treated as a constant in our study, and its value chosen for gas hydrate-bearing sediments is in accordance with earlier studies (Miyazaki *et al.* (2011), Lee *et al.* (2010a)). The Poisson ratio is of particular importance for the mechanical behavior under shear load and will be evaluated in more detail in upcoming studies by considering axial and lateral deformations along with bulk volume yielding.

Future combined experimental-numerical studies will focus on different gas hydrate formation procedures (i.e. formation of CH_4 -hydrates from over-saturated aqueous solutions) and different gas hydrate saturations. In order to further develop the mathematical model and numerical code, these studies will also be combined with tomographic techniques to monitor and resolve the local gas hydrate distribution, fluid migration, and sample heterogeneity.

APPENDIX

During the hydrate formation, a substantial volume of gas (≈ 180 mL) was trapped in the dead spaces (e.g., in pipes and manifolds). This gas interacted with the sample and significantly damped the pressure decay during to hydrate formation. We account for this effect in our simulation by introducing an additional source term for methane gas, $S_{ext}^{CH_4}$, in the mass balance Eqn.(1) for component $\kappa = CH_4$. The rationale behind adding this source term is the following:

- The dead space has a fixed volume of $V_{ext} = 180$ ml, and at the start of the experiment it is filled with methane gas. Mass of methane in the dead space is $m_{g,ext} = \rho_g(P_{ext}, T_{ext}) V_{ext}$, and the rate of change of gas mass is $\frac{\partial}{\partial t} m_{g,ext} = V_{ext} \frac{\partial}{\partial t} \rho_g(P_{ext}, T_{ext})$.
- Assuming that the pressure and temperature in the system (sample+dead space) equilibrate very fast, we can say $P_{ext} = P_g$ and $T_{ext} = T$. So, the rate of change of mass of methane gas in the dead space can be expressed as,

$$\frac{\partial}{\partial t} m_{g,ext} = V_{ext} \frac{\partial}{\partial t} \rho_g(P_g, T) = V_{ext} \frac{\rho_g(P_g, T)}{B_g} \frac{\partial}{\partial t} P_g$$

where, B_g is the bulk modulus of methane gas.

- Since the dead space+sample together form a closed system, any change of mass in the dead space must be due to transport of gas from dead space into the sample. Assuming that this transport is very fast, we can introduce a volumetric source term $S_{ext}^{CH_4}$ s.t.,

$$S_{ext}^{CH_4} = \frac{1}{V_s} \frac{\partial}{\partial t} m_{g,ext} = \frac{V_{ext}}{V_s} \frac{\rho_g(P_g, T)}{B_g} \frac{\partial}{\partial t} P_g$$

where, V_s is the sample volume.

In Fig10, the average gas pressure in the domain which is simulated without accounting for the gas in the dead spaces has been plotted. We can see clearly that the dead volume of the gas dampens the gas pressure decay significantly, and could not be ignored.

Acknowledgements We gratefully acknowledge the support for the first author by the German Research Foundation (DFG), through project no. WO 671/11-1. This work was further funded by the German Federal Ministries of Economy (BMWi) and Education and Research (BMBF) through the SUGAR project (grant No. 03SX250, 03SX320A & 03G0856A), by DEA Deutsche Erdöl AG, and the EU-FP7 project MIDAS (grant agreement no. 603418)

REFERENCES

(2008). Iapws industrial formulation 1997 for the thermodynamic properties of water and steam. In *International Steam*

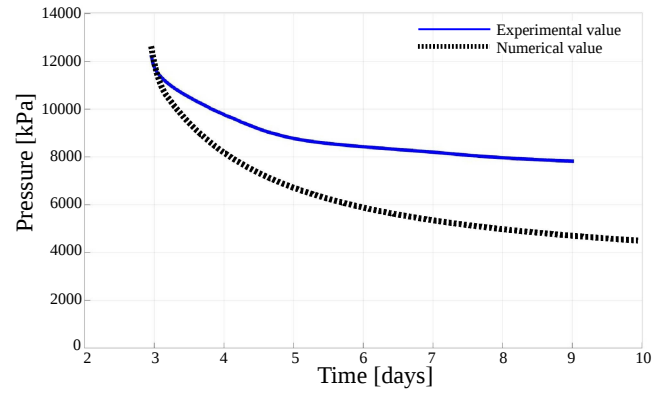


Fig. 10. Average gas pressure for the gas hydrate formation period without accounting for the gas trapped in the dead spaces.

Tables, Springer Berlin Heidelberg, pp. 7–150, doi:10.1007/978-3-540-74234-0-3.

- Anderson, B., Boswell, R., T.S., C., Farrell, H., Ohtsuki, S., White, M. & Zyrianova, M. (28 July - 1 August, 2014). Review of the findings of the ignik sikumi co2-ch4 gas hydrate exchange field trial. *Proceedings of the 8th International Conference on Gas Hydrates (ICGH8-2014), Beijing, China*.
- Archer, D., Buffett, B. & Brovkin, V. (2009). Ocean methane hydrates as a slow tipping point in the global carbon cycle. *Proc. Nat. Acad. Sci. USA* **106**, 20596–20601.
- Biot, M. (1941). General theory of three-dimensional consolidation. *J. Appl. Phys.* **12**, 155–164.
- Biot, M. & Willis, D. (1957). The elastic coefficients of the theory of consolidation. *J. Appl. Mech.* **24**, 594–601.
- Brugada, J., Cheng, Y., Soga, K. & Santamarina, J. (2010). Discrete element modelling of geomechanical behaviour of methane hydrate soils with pore-filling hydrate distribution. *Granular Matter* **12**, No. 5, 517–525, doi:10.1007/s10035-010-0210-y.
- Burdine, N. (1953). Relative permeability calculations from pore-size distribution data, technical report. *Technical report*, Petroleum Transactions, AIME.
- Burwicz, E., Rpke, L. & Wallmann, K. (2011). Estimation of the global amount of submarine gas hydrates formed via microbial methane formation based on numerical reaction-transport modeling and a novel parameterization of holocene sedimentation. *Geochim. Cosmochim. Acta* **75**, 4562–4576.
- Chaouachi, M., Falenty, A., Sell, K., Enzmann, F., Kersten, M., Habert, D. & Kuhs, W. F. (2015). Microstructural evolution of gas hydrates in sedimentary matrices observed with synchrotron x-ray computed tomographic microscopy. *Geochemistry, Geophysics, Geosystems* **16**, No. 6, 1711–1722, doi:10.1002/2015GC005811.
- Civan, F. (2000). Predictability of porosity and permeability alterations by geochemical and geomechanical rock and fluid interactions. In *SPE* 58746.
- David, C. (2013). Japanese test coaxes fire from ice. *Nature* **496**, 409 (April 25, 2013), doi:10.1038/496409a.
- Dedner, A., Flemisch, B. & Klöforn, R. (2012). *Advances in dune: Proceedings of the dune user meeting, held in october 6th–8th 2010 in stuttgart, germany*. SpringerLink : Bücher, Springer Berlin Heidelberg.
- Demmel, J., Gilbert, J. & Li, X. (September 1999). Superlu users guide. *Technical Report LBNL-44289*, Lawrence Berkeley National Laboratory, URL <http://crd-legacy.lbl.gov/>

- xiaoye/SuperLU/, last update: September 2007.
- Deusner, C., Bigalke, N., Kossel, E. & Haeckel, M. (2012). Methane production from gas hydrate deposits through injection of supercritical CO₂. *Energies* **5**, No. 7, 2112, doi:10.3390/en5072112.
- Esmailzadeh, F., Zeighami, M. E. & Fathi, J. (2008). 1-d modeling of hydrate decomposition in porous media. *International Journal of Chemical, Molecular, Nuclear, Materials and Metallurgical Engineering* **2**, No. 5, 45–51.
- Friend, D. G., Ely, J. F. & Ingham, H. (1989). Thermophysical properties of methane. *Journal of Physical and Chemical Reference Data* **18**, No. 2, 583–638, doi:http://dx.doi.org/10.1063/1.555828.
- Ghiassian, H. & Grozic, J. (2013). Strength behavior of methane hydrate bearing sand in undrained triaxial testing. *Marine and Petroleum Geology* **43**, 310 – 319, doi:http://dx.doi.org/10.1016/j.marpetgeo.2013.01.007.
- Gupta, S., Helmig, R. & Wohlmuth, B. (2015). Non-isothermal, multi-phase, multi-component flows through deformable methane hydrate reservoirs. *Computational Geosciences*, 1–26doi:10.1007/s10596-015-9520-9, URL <http://dx.doi.org/10.1007/s10596-015-9520-9>.
- Helmig, R. (1997). *Multiphase flow and transport processes in the subsurface: A contribution to the modeling of hydrosystems*. Berlin: Springer-Verlag.
- Himmelblau, D. M. (1964). Diffusion of dissolved gases in liquids. *Chem. Rev.* **64**, No. 5, 527–550.
- Hyodo, M., Yoneda, J., Yoshimoto, N., & Nakata, Y. (2013). Mechanical and dissociation properties of methane hydrate-bearing sand in deep seabed. *Soils Found.* **53**, No. 2, 299314, doi:10.1016/j.sandf.2013.02.010.
- Inada, N. & Yamamoto, K. (2015). Data report: Pressure coring and shipboard core handling in the nankai project. *Marine and Petroleum Geology* doi:doi:10.1016/j.marpetgeo.2015.02.023.
- Kamath, V. (1984). *Study of heat transfer characteristics during dissociation of gas hydrates in porous media*. Ph.D. thesis, Univ. of Pittsburgh, Pittsburgh, PA.
- Kamath, V. A. & Holder, G. D. (1987). Dissociation heat transfer characteristics of methane hydrates. *AIChE J.* **33**, 347–350.
- Kim, H., Bishnoi, P., Heidemann, R. & Rizvi, S. (1987). Kinetics of methane hydrate decomposition. *Chemical Engineering Science* **42**, No. 7, 1645 – 1653, doi:http://dx.doi.org/10.1016/0009-2509(87)80169-0.
- Klar, A., Soga, K. & NG, Y. (2010). Coupled deformation flow analysis for methane hydrate extraction. *Geotechnique* **60**, No. 10, 765776, doi:10.1680/geot.9.P.079-3799.
- Kvenvolden, K. (1993). Gas hydrates, geological perspective and global change. *Rev. Geophys.* **31**, 173–187.
- Lee, H., Seo, Y., Seo, Y.-T., Moudrakovski, I. & Ripmeester, J. (2003). Recovering methane from solid methane hydrate with carbon dioxide. *Angew. Chem. Int. Ed.* **42**, 5048–5051.
- Lee, J., Francisca, F., Santamarina, J. & Ruppel, C. (2010a). Parametric study of the physical properties of hydrate-bearing sand, silt, and clay sediments: 2. small-strain mechanical properties. *Journal of Geophysical Research* **115**(B11), 11p, doi:10.1029/2009jb006670.
- Lee, J. Y., Santamarina, J. C. & Ruppel, C. (2010b). Volume change associated with formation and dissociation of hydrate in sediment. *Geochemistry, Geophysics, Geosystems* **11**, No. 3, doi:10.1029/2009GC002667, q03007.
- M., H., Yanghui, L., Yoneda, J., Nakata, Y., N., Y. & Nishimura, A. (2014). Effects of dissociation on the shear strength and deformation behavior of methane hydrate-bearing sediments. *Marine and Petroleum Geology* **51**, 52 – 62, doi:10.1016/j.marpetgeo.2013.11.015.
- Milkov, A. V. (2004). Global estimates of hydrate-bound gas in marine sediments: how much is really out there? *Earth-Science Reviews* **66**, No. 34, 183 – 197, doi:http://dx.doi.org/10.1016/j.earscirev.2003.11.002.
- Miyazaki, K., Masui, A., Aoki, K., Sakamoto, Y., Yamaguchi, T. & Okubo, S. (2010). Strain-rate dependence of triaxial compressive strength of artificial methane-hydrate-bearing sediment. *International Journal of Offshore and Polar Engineering* **20**, No. 4, 256–264.
- Miyazaki, K., Masui, A., Sakamoto, Y., Aoki, K., Tenma, N. & Yamaguchi, T. (2011). Triaxial compressive properties of artificial methane-hydrate-bearing sediment. *J. Geophys. Res.-Solid Earth* **116**, B06102.
- Moridis, G., Collett, T., Boswell, R., Kurihara, M., Reagan, M., Koh, C. & Sloan, E. (2009). Toward production from gas hydrates: Current status, assessment of resources, and simulation-based evaluation of technology and potential. *SPE Reserv. Eval. Eng.* **12**, 745–771.
- Moridis, G., Collett, T., Pooladi-Darvish, M., Hancock, S., Santamarina, C., Boswell, R., Kneafsey, T., Rutqvist, J., Kowalsky, M. & Reagan, e. a., M.T. (2011). Challenges, uncertainties and issues facing gas production from gas hydrate deposits. *SPE Reserv. Eval. Eng.* **14**, 76–112.
- Ning, F., Yu, Y., Kjelstrup, S., Vlugt, T. J. H. & Glavatskiy, K. (2012). Mechanical properties of clathrate hydrates: status and perspectives. *Energy Environ. Sci.* **5**, 6779–6795.
- Park, Y., Kim, D.-Y., Lee, J.-W., Huh, D.-G., Park, K.-P., Lee, J. & Lee, H. (2006). Sequestering carbon dioxide into complex structures of naturally occurring gas hydrates. *Proc. Nat. Acad. Sci. USA* **103**, 12690–12694.
- Peng, D. Y. & Robinson, D. B. (1976). A new two-constant equation of state. *Industrial and Engineering Chemistry: Fundamentals* **15**, 59–64, doi:10.1021/i160057a011.
- Piñero, E., Marquardt, M., Hensen, C., Haeckel, M. & Wallmann, K. (2013). Estimation of the global inventory of methane hydrates in marine sediments using transfer functions. *Biogeosciences* **10**, No. 2, 959–975.
- Priest, J. A., Best, A. I. & Clayton, C. R. I. (2005). A laboratory investigation into the seismic velocities of methane gas hydrate-bearing sand. *Journal of Geophysical Research: Solid Earth* **110**, No. B4, doi:10.1029/2004JB003259.
- Priest, J. A., Rees, E. V. L. & Clayton, C. R. I. (2009). Influence of gas hydrate morphology on the seismic velocities of sands. *Journal of Geophysical Research: Solid Earth* **114**, No. B11, doi:10.1029/2009JB006284.
- Reagan, M., Moridis, G., Johnson, J., Pan, L., Freeman, C., Pan, L., Boyle, K., Keen, N. & Husebo, J. (2015). Field-scale simulation of production from oceanic gas hydrate deposits. *Transport in Porous Media* **108**, No. 1, 151–169, doi:10.1007/s11242-014-0330-7.
- Rockhold, M., Yarwood, R., Niemet, M., Bottomley, P. & Selker, J. (2002). Considerations for modelling bacterial-induced changes in hydraulic properties of variably saturated porous media. *Advances in Water Resources* **25**, 477–495.
- Roder, H. (1985). Thermal conductivity of methane for temperatures between 110 K and 310 K with pressures up to 70 MPa. *Journal of Thermophysics* **6**, No. 2, 119–142.

- Rutqvist, J. (2011). Status of the tough-flac simulator and recent applications related to coupled fluid flow and crustal deformations. *Computers & Geosciences* **37**, 739750, doi:10.1016/j.cageo.2010.08.006.
- Rutqvist, J., Moridis, G., Grover, T. & Collett, T. (2009). Geomechanical response of permafrost-associated hydrate deposits to depressurization-induced gas production. *J. Pet. Sci. Eng.* **67**, 1–12.
- Rutqvist, J., Moridis, G., Grover, T., Silpnargmlert, S., Collett, T. & Holdich, S. (2012). Coupled multiphase fluid flow and wellbore stability analysis associated with gas production from oceanic hydrate-bearing sediments. *Journal of Petroleum Science and Engineering* **9293**, 65 – 81, doi:http://dx.doi.org/10.1016/j.petrol.2012.06.004.
- Sander, R. (retrieved February 23, 2015). Henry's law constants. In *NIST Chemistry WebBook* (Linstrom, P. & Mallard, W., eds.), No. 69 in NIST Standard Reference Database, Gaithersburg MD, 20899: National Institute of Standards and Technology, URL <http://webbook.nist.gov>.
- Santamarina, J., Dai, S., Terzariol, M., Jang, J., Waite, W., Winters, W., Nagao, J., Yoneda, J., Konno, Y., Fujii, T. & Suzuki, K. (2015). Hydro-bio-geomechanical properties of hydrate-bearing sediments from nankai trough. *Marine and Petroleum Geology*, –doi:http://dx.doi.org/10.1016/j.marpetgeo.2015.02.033.
- Santamarina, J. C. & Ruppel, C. (2010). The impact of hydrate saturation on the mechanical, electrical, and thermal properties of hydrate-bearing sand, silts, and clay in geophysical characterization of gas hydrates. *Geo-phys. Dev. Ser., edited by M. Riedel, C. Willoughby, and S. Chopra, Soc. of Explor. Geophys., Tulsa, Oklahoma, USA* **14**, 373–384.
- Schoderbek, D., Farrell, H., Hester, K., Howard, J., Raterman, K., Silpnargmlert, S., Martin, K., Smith, B. & Klein, P. (October 1, 2008–June 30, 2013). Conocophillips gas hydrate production test final technical report. *Technical report*, ConocoPhillips, URL <http://www.netl.doe.gov>.
- Sloan, E. & Koh, C. (2007). *Clathrate hydrates of natural gases, third edition*. Chemical Industries, CRC Press.
- Soga, K., Lee, S., Ng, M. & Klar, A. (2006). Characterisation and engineering properties of methane hydrate soils. In *Characterization and Engineering Properties of Natural Soils* (Tan, e. a., T.S., ed.), 4 edn., London: Taylor and Francis, pp. 2591–2642.
- Song, Y., Yu, F., Li, Y., Liu, W. & Zhao, J. (2014). Mechanical property of artificial methane hydrate under triaxial compression. *Journal of Natural Gas Chemistry* **19**, 246–250.
- Statter, J. & Bird, R. (June 1958). Calculation of diffusion coefficient of dilute gases and of the self diffusion coefficient of dense gases. *AIChE J.* **4**, No. 2, 137–142.
- Stern, L. A., Circone, S., Kirby, S. H. & Durham, W. B. (2003). Temperature, pressure, and compositional effects on anomalous or "self" preservation of gas hydrates. *Canadian Journal of Physics* **81**, No. 1-2, 271–283, doi:10.1139/p03-018, <http://dx.doi.org/10.1139/p03-018>.
- Sultan, N. & Garziglia, S. (2011). Geomechanical constitutive modelling of gas-hydrate-bearing sediments. In *The 7th International Conference on Gas Hydrates (ICGH 2011)*.
- Sun, F. & Mohanty, K. (2006). Kinetic simulation of methane hydrate formation and dissociation in porous media. *Chemical Engineering Science* **61**, 3476–3495.
- Terzaghi, K. (1925). *Erdbaumechanik auf bodenphysikalischer grundlage*. Wien: F. Deuticke.
- Verruijt, A. (2008). *Encyclopedia of hydrological sciences*, Ch. Consolidation of soils. Chichester, UK: Wiley, doi:10.1002/0470848944.hsa303.
- Waite, W. F., Santamarina, J. C., Cortes, D. D., Dugan, B., Espinoza, D. N., Germaine, J., Jang, J., Jung, J. W., Kneafsey, T. J., Shin, H., Soga, K., Winters, W. J. & Yun, T. S. (2009). Physical properties of hydrate-bearing sediments. *Reviews of Geophysics* **47**, No. 4, doi: 10.1029/2008RG000279.
- Winters, W., Waite, W., Mason, D., Gilbert, L. & Pecher, I. (2007). Methane gas hydrate effect on sediment acoustic and strength properties. *Journal of Petroleum Science and Engineering* **56**, No. 13, 127 – 135, doi:http://dx.doi.org/10.1016/j.petrol.2006.02.003, natural Gas Hydrate / ClathrateThe Major Organic Carbon Reserve of the Earth.
- Yamamoto, K. (2013). Japan completes first offshore methane hydrate production test - methane successfully produced from deepwater hydrate layers. fire in the ice: Department of energy, office of fossil energy, national energy technology laboratory. *Methane Hydrate News Letter* **13**, No. 1-2.
- Yamamoto, K. (2015). Overview and introduction: pressure core-sampling and analyses in the 2012-2013 mh21 offshore test of gas production from methane hydrates in the eastern nankai trough. *Marine and Petroleum Geology* .
- Yoneda, J., Masui, A., Konno, Y., Jin, Y., Egawa, K., Kida, M., Ito, T., Nagao, J. & Tenma, N. (2015). Mechanical properties of hydrate-bearing turbidite reservoir in the first gas production test site of the eastern nankai trough. *Marine and Petroleum Geology* doi: 10.1016/j.marpetgeo.2015.02.029.
- Yousif, M. (1991). Experimental and theoretical investigation of methane-gas-hydrate dissociation in porous media. *SPE Reserv. Eng.* , 69–76.
- Yun, T., Santamarina, J. & Ruppel, C. (2007). Mechanical properties of sand, silt, and clay containing tetrahydrofuran hydrate. *J. Geophys. Res.* **112**, B04106, doi:10.1029/2006JB004484.